Energy & Environmental Science

Accepted Manuscript

ROYAL SOCIETY OF CHEMISTRY

www.rsc.org/ees

Journal Name RSCPublishing

ARTICLE

Organohalide Lead Perovskites for Photovoltaic Applications

Cite this: DOI: 10.1039/x0xx00000x

Received 00th January 2012,
Accepted 00th January 2012

DOI: 10.1039/x0xx00000x

www.rsc.org/

Peng Gao*, Michael Grätzel, and Mohammad K. Nazeeruddin*

There are only few semiconducting materials that have been shaping the progress of third generation photovoltaic cell as much as perovskites. Although they are deceivingly simple in structure, the archetypal AMX_3-type perovskites have a built-in potential for complexity and surprising discoveries. Since 2009, a small and somewhat exotic class of perovskites, which are quite different from the common rock-solid oxides perovskite, turned over a new leaf in solar cell research. Highlighted as one of the major scientific breakthroughs of the year 2013, the power conversion efficiency of the title compound hybrid organic–inorganic perovskite has now exceeded 16%, making it competitive with thin-film PV technology. In this Minireview, a brief history of perovskite materials for photovoltaic application is reported, the current state-of-the-art is distilled and the basic working mechanisms have been discussed. By analyzing the attainable photocurrent and photovoltage, realizing perovskite solar cells with 20% efficiency for a single junction, and 30% for a tandem configuration on c-Si solar cell would be realistic.

Introduction

Generally, perovskite refers to a calcium titanium oxide mineral species composed of calcium titanate, with the chemical formula of $CaTiO_3$. The mineral was discovered in the Ural Mountains of Russia by Gustav Rose in 1839 and is named after Russian mineralogist Lev Perovski.[1] Later on, the word 'perovskite' was borrowed to describe any material with the same type of crystal structure as calcium titanium oxide ($CaTiO_3$), known as the perovskite structure. The compounds of perovskite family exist extensively in nature, and the magnesium silicate perovskite ($MgSiO_3$) is the most abundant mineral in the earth mantle.[2,3]

The general chemical formula for purebred perovskite compounds is AMX_3, where 'A' and 'M' are two cations of very different sizes, and X is an anion that bonds to both. Oxide perovskites (AMO_3) are formed from divalent A^{II} (Mg^{2+}, Ca^{2+}, Sr^{2+}, Ba^{2+}, Pb^{2+}) and tetravalent M^{IV} (Ti^{4+}, Si^{4+}, Fe^{4+}) elements with O as the anion. The ideal cubic-symmetry structure has the M cation in 6-fold coordination, surrounded by an octahedron of anions (MX_6), and the A cation in 12-fold cuboctahedral coordination. (Figure 1a and 1b) The relative ion size requirements for stability of the cubic structure are quite stringent, so slight buckling and distortion can produce several lower-symmetry distorted versions, in which the coordination numbers of 'A' cations, 'M' cations or both are reduced. Many physical properties of perovskites depend crucially on the details of these distortions, particularly the electronic, magnetic and dielectric properties, which are so important for many of the applications of perovskite materials. For example, the distortions as a consequence of cation substitution can be used to fine tune physical properties exhibited by perovskites. For perovskites, the measure of the mismatch between the average equilibrium A-X and M-X bond lengths is expressed by tolerance factor $t = (R_M + R_X)/\sqrt{2}(R_A + R_X)$ (where R_A, R_M and R_X are the ionic radii of A, M and X, respectively).

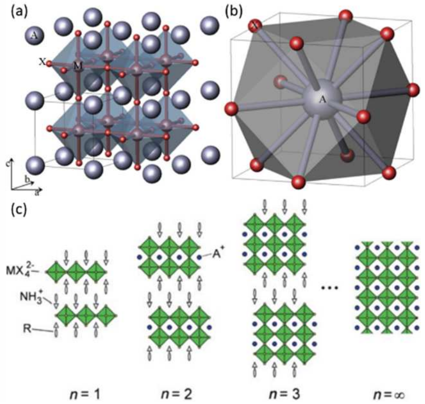

Figure 1. (a) Crystal structure of cubic perovskite of general formula ABX_3; (b) Twelve-fold coordination of the A-site cation; (c) The <100>-oriented hybrid perovskite series with general formula of $(RNH_3)_2A_{n-1}M_nX_{3n+1}$. The thicknesses of inorganic slabs increase and toward 3D structure with increasing n. Reproduced from Ref. 4.

The first observation of photocurrents in oxide perovskite - $BaTiO_3$ can date back to 1956. Following that, similar phenomenon was observed in $LiNbO_3$, which was attributed to the presence of internal fields due to space charge at the crystal surfaces - ferroelectricity.[5] Enlightened by these pioneering works, researchers started to explore the potential of photovoltaic application in these oxide perovskites.[6-18] The physical mechanism of photovoltaic effect in ferroelectrics is not completely understood. Possible explanation is schematically illustrated in Figure 2. In these materials, the strong inversion symmetry breaking leading to polarization-induced internal electric field promotes the desirable separation of photo-excited carriers and allows voltages higher than the bandgap, which may enable efficiencies beyond the maximum possible in a conventional p-n junction solar cell. For example, in doped ferroelectric $LiNbO_3$ crystals a large saturation photovoltage in excess of 1000 V was demonstrated.[17] However, the previously obtained efficiency of photovoltaic effect in oxide perovskites is very low, typically from the order of 10^{-7}-10^{-5} to less than 1%.[8]

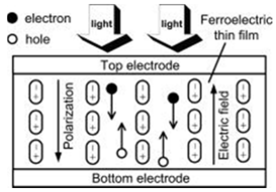

Figure 2. Schematic illustration of physical mechanism of photovoltaic effect in a ferroelectric. Reprinted with permission. [10]

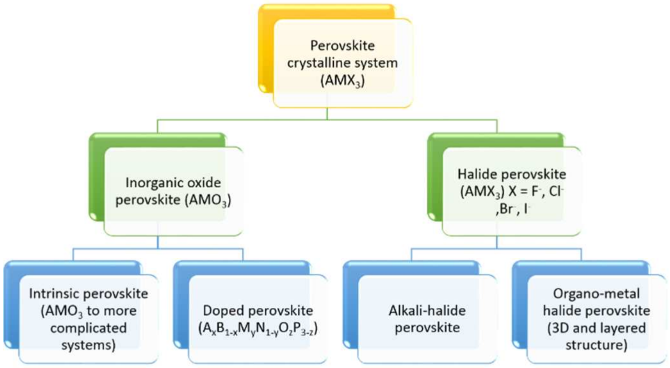

Figure 3. Crystalline systems of perovskite type.

Halide perovskite (AMX_3) represents a big collateral series of perovskite family and it is reasonable to divided them roughly into alkali-halide perovskite and organo-metal halide perovskite. (Figure 3) The first category is mainly formed from monovalent alkali metal A^I (Li^+, Na^+, K^+, Rb^+, Cs^+) and divalent M^{II} (Be^{2+}, Mg^{2+}, Ca^{2+}, Sr^{2+}, Ba^{2+}, Zn^{2+}, Ge^{2+}, Sn^{2+}, Pb^{2+}, Fe^{2+}, Co^{2+}, Ni^{2+}) with X representing halogen anions (F^-, Cl^-, Br^-, I^-). There was no report relating halide perovskite materials to solar absorber until 1980,[19] when Salau reported new compound $KPbI_3$ (potassium lead iodate) having an absorption edge (direct energy gaps between 1.4 and 2.2 eV) that matches the solar spectrum. To the best of our knowledge, this is the first time that the halide perovskite material has been identified for photovoltaic application. Considering Schoiject's[20] proposition on the requirements of new materials for solar photovoltaic cells, the author suggested the potential use of $KPbI_3$ as a new solar cell material with an optimum theoretical efficiency of 36% and operating temperature of 220°C.[21] Though the author prepared the alloys with desired band gap by simply grinding together the powders of PbI_2 and KI, no real solar cell device was demonstrated based on this alkali metal halide perovskite material.

Distinct from the inorganic oxide perovskites and alkali-metal halide perovskite, for the past 20 years, the organometal halide perovskites (AMX_3) features a relatively young but also extensively studied crystalline families of hybrids, consisting of a wide range of organic cations (A: aliphatic or aromatic ammonium) and divalent metal cations (M: Cu^{2+}, Ni^{2+}, Co^{2+}, Fe^{2+}, Mn^{2+}, Pd^{2+}, Cd^{2+}, Ge^{2+}, Sn^{2+}, Pb^{2+}, Eu^{2+}, etc.). (Figure 3) Among these combinations, perovskites containing metal halides in the fourth main group (4A, including Ge^{2+}, Sn^{2+}, Pb^{2+}) attracted more interest due to their good optoelectronic properties and potential for low-temperature device fabrication.[22-25] Depending on the character of ammonium cation, the general formula for a typical <100> single or multilayer organometal halide perovskite can be written as $(RNH_3)_2A_{n-1}M_nX_{3n+1}$ (where A = CH_3NH_3 but may be any other small cation).[26, 27] (Figure 1c) When n = 1, a single inorganic layer is encountered. As n increases so does the thickness of the inorganic sheet. Hence as n ⟶ ∞ the dimensionality ⟶ 3D. The ending of this process is narrowed band gap and/or increased mobility of charges within the layers.[28-30] The focus of this minireview will be on the solar cell application of 3D perovskite materials.

Although these class of materials have been widely studied for decades,[31, 32] initial interest was focused on their photo- or ionic conductivity and semiconducting properties for organic light-emitting diodes (OLEDs) and thin film transistors (TFTs) applications.[33, 34] At the same time, unlike the intensive studies on tin(II)-based halide perovskite, lead(II)-based halide perovskites have received less attention due to much decreased metallic behavior and charge carrier mobility with respect to use in superconductor or TFT devices.

In the spring of 2009, organometal halide perovskites made a re-entry into the literature in the name of visible-light sensitizers for photovoltaic cells.[35] In this report, Miyasaka et al pioneered the first perovskite solar cells based on mesoporous TiO_2 photoanodes that were sensitized with $CH_3NH_3PbX_3$ (X = I, Br). However, the resulting photo to current conversion efficiencies (PCEs) were only moderate (η = 3.81% for the triiodide and 3.13% for the tribromide), and the cell stabilities were poor in a liquid electrolyte configuration. Subsequently, in 2011 Park et al. fabricated again liquid dye sensitized solar cells (DSSCs) using ca. 2-3 nm sized $CH_3NH_3PbI_3$ ($MAPbI_3$) nanocrystals with iodide redox shuttle and bumped up the conversion efficiency of the triiodide cell to 6.54% at 1 sun illumination.[36] The improvement is believed to be due to the optimized titania surface and substitution of the DMF solvent by γ-butyrolactone (GBL). In both cases the perovskite absorber were regarded as quantum dots (QDs) deposited on TiO_2 although the absorbers dissolved or decomposed in the liquid electrolyte and the cells rapidly degraded within a few minutes. A schematic of the perovskite-sensitized titania and the spectral response of the ensuing solar cells is shown in Figure 4.

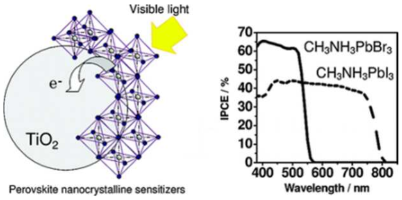

Figure 4. A schematic illustration of perovskite-sensitized TiO_2 undergoing photoexcitation and electron transfer (left). The incident photon-to-electron conversion efficiency (IPCE) spectra for perovskite-sensitized solar cells. Reprinted with permission. [35]

When the organometal halide perovskites cells were facing the hitch of poor stability, alkali metal halide perovskite - fluorine-doped $CsSnI_3$ was adopted by Kanatzidis and co-workers in 2012 as p-type solid hole transporting materials (HTM) in a traditional dye-sensitized architecture with N719 as the absorber. This is the first time that the use of a perovskite material as the HTM in a solid state DSSC (ssDSSC) with efficiencies reaching approximately 10.2 %, which revived the concept of all-solid-state inorganic solar cells and indicated the possibility that perovskite materials could be good HTM candidates.[37, 38] For solid-state sensitized solar cells, this represented a big step forward in performance in comparison to the best-reported ssDSSCs before, which exhibited just over 7% efficiency. [37]

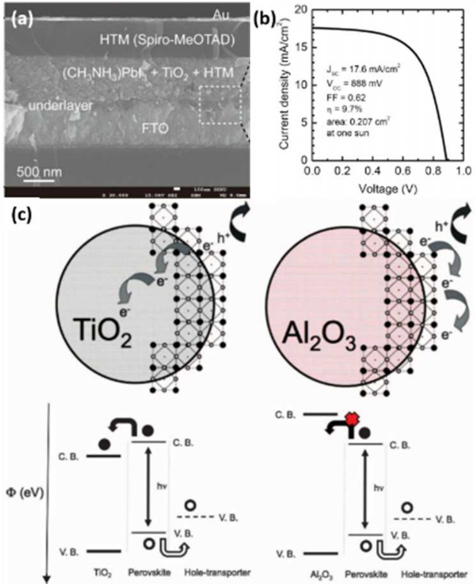

Figure 5. (a) Cross-sectional SEM images; (b) photocurrent density as a function of forward bias. Reprinted with permission. [39] (c) Charge transfer and charge transport in a perovskite-sensitized TiO_2 solar cell (left) and a non-injecting Al_2O_3 -based solar cell (right). Below are the respective energy landscapes with electrons shown as solid circles and holes as open circles. Reprinted with permission. [40]

Next breakthrough came in late 2012, when M. Grätzel and co-workers teamed up with N. G. Park, used $MAPbI_3$ as a light harvester in combination with the solid hole conductor 2,2',7,7,'-tetrakis-(*N*,*N*-dimethoxyphenyl-amine)-9,9'-spirobifluorene (spiro-MeOTAD)[41] on mesoporous TiO_2 (m-TiO_2), which led to a PCE of 9.7%.[39] (Figure 5a,b) Soon after that, H. Snaith in collaboration with T. Miyasaka discovered that in "meso-superstructured" solar cells the n-type mesoporous oxide can be replaced by an inert scaffold, such as Al_2O_3, onto which $CH_3NH_3PbI_{3-x}Cl_x$ and spiro-MeOTAD were coated.[40] (Figure 5c) The authors claimed that compared with the cells with m-TiO_2, the use of Al_2O_3 scaffold avoids the voltage drop associated with the occupation of the TiO_2 band-tails and generates increased open circuit voltage (V_{OC}) values as high as 1.13 V and an efficiency of 10.9%. This result established that the perovskite materials can also behave as n-type semiconductor. But it seems that in the absence of an m-TiO_2 layer, a qualified compact TiO_2 (c-TiO_2) is still detrimental in a well-performing device.

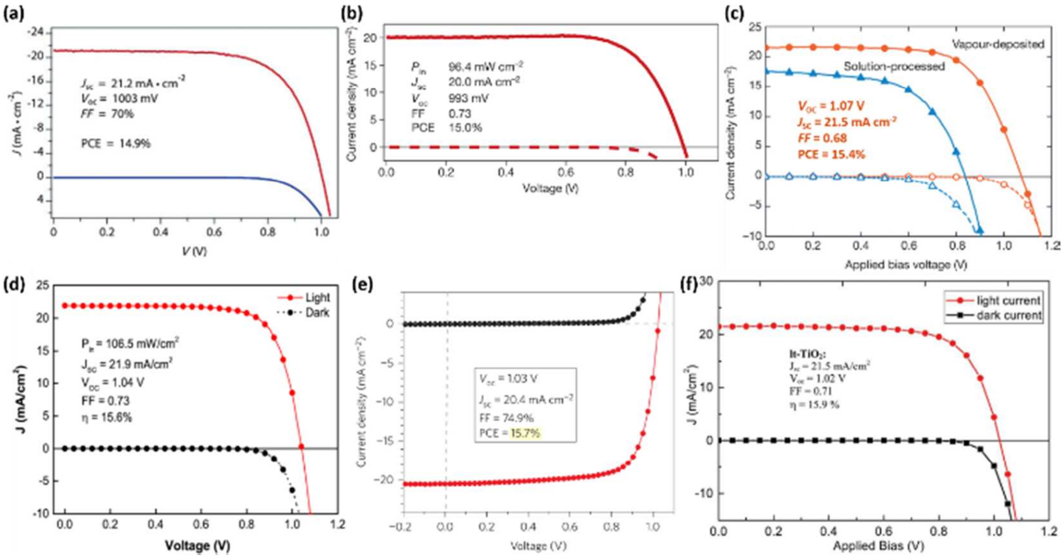

Figure 6. Measured current-voltage curves and performance characteristics for record organometal halide perovskites solar cells. (a) m-TiO_2/$NHCH_2NH_3PbI_3$/spiro-MeOTAD. Reprinted with permission. [42] (b) m-TiO_2/$CH_3NH_3PbI_3$/spiro-MeOTAD. Reprinted with permission. [43] (c) c-TiO_2/$CH_3NH_3PbI_{3-x}Cl_x$/spiro-MeOTAD. Reprinted with permission. [44] (d) Graphene-TiO_2 nanocomposites/meso-Al_2O_3/$CH_3NH_3PbI_{3-x}Cl_x$/spiro-MeOTAD. Reprinted with permission. [45] (e) c-ZnO/$CH_3NH_3PbI_3$/spiro-MeOTAD. Reprinted with permission. [46] (f). lt-TiO_2/$CH_3NH_3PbI_{3-x}Cl_x$/spiro-MeOTAD. Reproduced from Ref. 47.

Since the middle of 2013, several milestones in PCE improvement were witnessed due to the innovation of cell fabrication technique, which leads the organometal halide perovskites based solar cells into the era of 15%. (Figure 6) First came the introduction of a sequential deposition method (SDM) for the fabrication of perovskite on m-TiO_2 film, which gave a PCE of 15% and a certified value of 14.1% with high reproducibility,[43, 48] then came the planar heterojunction perovskite solar cell fabricated by vapor deposition which demonstrated 15.4% PCE and matched the 15% efficiency record of the mesoporous cell.[44] After that, a series of eye catching PCE values were reported: 15.6%[45], 15.7%[46] and 15.9%[47] and by the end of 2013, 16.2% efficiency was certified as well.[49] The fast development has triggered tremendous research interest following by rapid and continuous improvements in whole perspective of the relative PV devices and started discussions about the underlying principles and the potential for further improvement of efficiency.[46, 50-55] A thorough retrospect of the metal halide perovskites revealed the materials' excellent optical, electrical and mechanical properties[56-63] along with solution processability. The remarkable synergistic achievements[64-69] on devices from both materials science and device engineering promise further breakthroughs in this field of study. Currently, researchers from all of the world are working to broaden the cells' appeal by tailoring their chemical compositions to further boost electrical output, by improving processing methods and stability, and by figuring out why these solar cells perform so unexpectedly well. (Table 1)

Band gap engineering of perovskite materials

Choices of materials for solar light harvesting are diverse, but the good candidates all share one merit: broad and strong absorption over the visible to near infrared region of the solar spectrum. It is believed that semiconductors with band gap below 1.1 eV are suitable for solar light absorber. This band gap determines the strength (voltage) of the electric field, and when it's too low, then the cell will collect extra current (by absorbing more photons), but at the cost of having a small voltage. The optimal band gap, balancing these two effects, is around 1.4 eV for a solar cell made from a single material.[70] According to the studies on perovskite crystals, scientists found that the band gap of perovskite material will decrease with a) increase of the dimensionality of $MO(X)_6$ network[71]; b) increase of the angle of M-O(X)-M ($\leqslant 180^o$) bonds[29]; c) decrease of the electronegativity of anions[72-76]; d) decrease of the difference in effective electronegativity between metal (M) cation and the anion. While the last two parameters are directly controlled by the nature of the elemental atoms (molecules), the first two are also influenced by extraneous factors e.g. temperature and/or pressure. Due to space constraints in paragraph, we will only discuss the band-gap tuning strategy above room temperature and under atmospheric conditions.

Table 1. A summary of published typical results of perovskite solar cells performance parameters with different device fabrication method and configuration.

Perovskite	**Deposition/solvent**	**Blocking layer formation**	**ETM^a**	**HTM^b/Redox**	**Jsc^c [mA/cm]**	**Voc^d [V]**	***FF*^{e} [%]**	**PCE^f [%]**	**Mask area [cm^2]**	**Ref**
$MAPbI_3$	OSPD^g/DMF^h	$TiCl_4$ treatment	m-TiO_2^{i}	I^-/I_3^-	11.0	0.61	57	3.81	0.238	35
$MAPbI_3$	OSPD/GBL^j	Spin pyrolysis^k	m-TiO_2/$Pb(NO_3)_2$ treatment	I^-/I_3^-	15.82	0.706	58.6	6.54	0.309	36
$MAPbI_3$	OSPD/GBL	Spin pyrolysis	m-TiO_2/$TiCl_4$	Spiro^l	17.6	0.888	62	9.7	0.27	39
$MAPbI_3$	OSPD/GBL	Spray pyrolysis^m	TiO_2 nanosheet/$TiCl_4$	no	16.1	0.632	57	5.5	0.12	55
$MAPbI_3$	OSPD/GBL	Spray pyrolysis	m-TiO_2/m-ZrO_2/m-carbon	no	12.4	0.878	61	6.64	0.125 ⊂ 0.5	77
$MAPbI_3$	OSPD/GBL/DMF	$TiCl_4$ Treatment	m-TiO_2/$TiCl_4$	no	18.8	0.712	60	8.0	0.09	78
$MAPbI_3$	SDM^n/DMF	Spin pyrolysis	m-TiO_2/$TiCl_4$	no	17.8	0.905	65	10.5	0.08	79
$MAPbI_3$	SDM/DMF	Spray pyrolysis	Perovskite on m-ZrO_2	Spiro	17.3	1.07	59	10.8	0.2	80
$MAPbI_3$	SDM/DMF	Spray pyrolysis	m-TiO_2	Spiro	20.0	0.993	73	15.0	0.285	43
$MAPbI_3$	OSPD/GBL	Spray pyrolysis	m-TiO_2	PTAA	16.5	0.997	72.7	12.0	0.096	81
$MAPbI_3$	VASP^o/DMF	Spin pyrolysis	Perovskite	Spiro	19.8	0.924	66.3	12.1	0.12	82
$MAPbI_3$	SDM/DMF	ZnO nanoparticle	Perovskite	Spiro	20.4 (13.4Fl^p)	1.03 (1.03 Fl)	74.9 (73.9 Fl)	15.7 (10.2 Fl)	0.07065	46
$MAPbI_3$	SDM/DMF	$TiCl_4$ solution dipping	Perovskite	Spiro	19.8	1.05	64	13.7	0.285	83
$MAPbI_3$	DSVD^q	PolyTPD^r	PCBM^s	PEDOT:PSS	16.12	1.05	67	12.04	0.09	84
$MAPbI_3$	DSVD	PolyTPD	PCBM	PEDOT:PSS	14.3 (Fl)	1.04 (Fl)	47 (Fl)	7% (Fl)	0.12	85
$MAPbI_3$	OSPD/DMF	no	PCBM	PEDOT:PSS	10.8	0.91	76	7.41	0.07	86
$MAPb(I_{1-x}Br_x)_3$	OSPD/DMF/GBL	Spray pyrolysis	m-TiO_2	PTAA^r	18.0	0.87	66	12.3	0.16	87
$MAPbI_{3-x}Cl_x$	OSPD/DMF	Spray pyrolysis	Perovskite on m-Al_2O_3	Spiro	17.8	0.98	63	10.9	0.09	40
$MAPbI_{3-}$	OSPD/DMF	Spin pyrolysis	Perovskite on m-	Spiro	18.0	1.02	67	12.3	0.09	54

$_x$Cl$_x$			Al_2O_3							
$MAPbI_{3-x}Cl_x$	DSVD	Spin pyrolysis	Perovskite	Spiro	21.5	1.07	68	15.4	0.076	44
$MAPbI_{3-x}Cl_x$	OSPD/DMF	Graphene/TiO_2 nanocomposites	Perovskite on m-Al_2O_3	Spiro	21.9	1.04	73	15.6	0.0625	45
$MAPbI_{3-x}Cl_x$	OSPD/DMF	TiO_2 nanoparticles colloidal	Perovskite on m-Al_2O_3	Spiro	21.5	1.02	71	15.9	0.0625 ⊂0.12	47
$MAPbI_{3-x}Cl_x$	OSPD/DMF/	Spin pyrolysis	Perovskite	Spiro	20.3	0.89	64	11.4	0.09	88
$MAPbI_2Cl$	OSPD/DMSO[t]	Spin pyrolysis	Perovskite	P3HT[u]	21.3	0.932	54.4	10.8	0.03~0.05	89
$MAPbI_{3-x}Cl_x$	OSPD/DMF	Spin pyrolysis	Fullerene/m-TiO_2	Spiro	19.6	0.84	72	11.7	0.09	90
$MAPbI_{3-x}Cl_x$	OSPD/DMF	no	PCBM/TiOx (120°C)	PEDOT:PSS	16 (14.4 Fl)	0.9 (0.88 Fl)	66 (51 Fl)	9.8 (6.4Fl)	0.08	91
$MAPbI_{3-x}Cl_x$	OSPD	no	PCBM	PEDOT:PSS	18.5 (16.5 Fl)	0.87 (0.86 Fl)	72 (64 Fl)	11.5 (9.2Fl)	0.1	92
$MAPbBr_3$	OSPD/DMF	$TiCl_4$ treatment	m-TiO_2	Br^-/Br_3^-	5.57	0.96	59	3.13	0.238	35
$MAPbBr_3$	OSPD/DMF	Spin pyrolysis	m-TiO_2	PCBTDPP[v]	4.47	1.16	59	3.04	0.1134	93
$MAPbBr_3$	OSPD/DMF	Spin pyrolysis	Perovskite on m-Al_2O_3	PDI[w]	1.08	1.30	40	0.56	<0.03	52
$MAPbBr_3$	OSPD/DMF	Spray pyrolysis	m-TiO_2	PTAA	5.0	1.13	74	4	0.16	87
$MAPbBr_{3-x}Cl_x$	OSPD/DMF	pyrolysis	Perovskite on m-Al_2O_3	CBP[x]	4.0	1.50	46	2.7	0.16 ⊂ 0.24	94
$FAPbI_3$	OSPD/DMF/HI	pyrolysis	Perovskite	Spiro	23.3	0.94	65	14.2	0.0625	95
$FA_{0.4}/MA_{0.6}PbI_3$	SDM	$TiCl_4$ Spin-coating	m-TiO_2	Spiro	21.2	1.003	70	14.9	0.285	42
$MASn_{0.5}Pb_{0.5}I_3$	OSPD/DMF	Spray pyrolysis	m-TiO_2	P3HT	20.04	0.42	50	4.18	0.16	96

a. ETM, electron transporting materials; b. HTM hole transporting layers; c. J_{SC}: short circuit current; d. V_{OC}: open circuit voltage; e. FF: fill factor; f. PCE: photon to current efficiency; g. One step precursor deposition; h. DMF: dimethylformamide; i. Mesoporous TiO_2 with 500°C sinter with/without $TiCl_4$ treatment; j. GBL: gamma-butyrolactone; k. Spin coating Ti(IV) bis(ethyl acetoacetato)-diisopropoxide precursor and pyrolysis at 450°C to 500°C. l. 2,2',7,7'-tetrakis(*N*,*N'*-di-p-methoxyphenylamine)-9,9'-spirobifluorene (spiro-OMeTAD); m. Spray pyrolysis Ti(iv) precursor 300°C-500°C; n. Sequential deposition method; o. Vapor-assisted solution process; p. FL: results based on a flexible substrate; q. Dual-source vapor deposition; r. PolyTPD and PTAA: polytriarylamine derivatives; s. PCBM: phenyl-C_{61}-butyric acid methyl ester; t. DMSO: dimethyl sulfoxide; u. P3HT: poly(3-hexylthiophene-2,5-diyl); v. PCBTDPP: poly[*N*-9-hepta-decanyl-2,7-carbazole-alt-3,6-bis-(thiophen-5-yl)-2,5-dioctyl-2,5-dihydropyrrolo[3,4-]pyrrole-1,4-dione]; w. PDI: perylene-diimide; x. 4,4'-bis(*N*-carbazolyl)-1,1'-biphenyl.

Oxide perovskite (AMO_3)

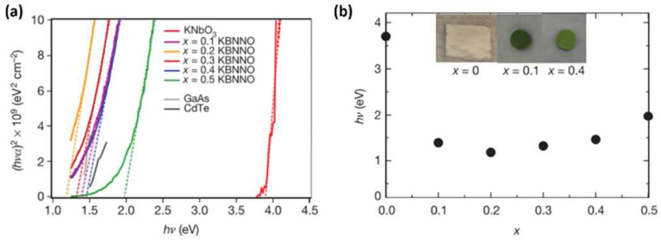

Figure 7. (a) Ellipsometry measurements for KBNNO oxides with x = 0.0 - 0.5, showing bandgaps from 1.18 eV to 3.8 eV. This makes KBNNO promising for visible solar light absorption. (b) Bandgap values versus BNNO fraction. Also shown are images of the $KNbO_3$ and KBNNO pellets for x = 0.1 and x = 0.4 compositions. Reprinted with permission. [18]

The typical oxide perovskite normally refer to alkaline earth metal titanate ($ATiO_3$, A: Ca, Sr, Ba) and are colorless wide band gap (3 - 5 eV) solid due to the large difference in electronegativity between the oxygen and titanium atoms. The electronic structure of simple perovskite-type oxides near the Fermi level is formed mainly by mixing of frontier *d*-orbitals of the transition metal and 2*p*-orbitals of oxygen. The top of the valence band is represented mainly by oxygen non-bonding 2*p*-orbitals, whereas the bottom of the conduction band is formed by the anti-bonding 2*p*-*nd* orbitals of both atoms. By modifying the composition of the material according to the rules mentioned above, one low bandgap for an oxide perovskite E_g = 2.7 eV has been obtained for $BiFeO_3$ and the recently fabricated $LaCoO_3$-doped $Bi_4Ti_3O_{12}$ films.[11, 97] This made $BiFeO_3$ the subject of a number of investigations for photovoltaic applications.[6, 9, 98] In 2013, A. M. Rappe and P. K. Davies[18] showed the first strongly visible-light-absorbing ferroelectric perovskite material $[KNbO_3]_{1-x}[BaNi_{1/2}Nb_{1/2}O_{3-\delta}]_x$

(KBNNO) with the bandgaps in the range of 1.1– 2.0 eV. (Figure 7) This study opened up the possibility of the use of oxide perovskites as solar absorber layers and carrier separators in practical photovoltaics.

Halide perovskite (AMX_3)

Similar to their oxide perovskite counterparts, halide perovskite (AMX_3) can easily achieve bandgap tuning by varying the combination of all the three cationic and anionic components. It is known from first-principles study that the electronic structure of halide perovskite is dominated by character of M-X bond: the valence-band maximum is characterized as an antibonding hybrid state of the M-m*s* (Pb: m = 6) and the X-n*p* (n = 3 - 5) orbitals in the M-X chains. The conduction-band minimum is characterized as a non-bonding hybrid state of the M-m*p* (Pb: m = 6) and the X-n*p* (n = 3 - 5) orbitals.[30, 63]

Influence of A cation

It has been proposed that in this system, the A cation does not play a major role in determining the band structure but acts to make charge compensation within the lattice.[99] Nevertheless, it can influence the optical properties by deforming the MX_6^{4-} octahedron network due to the variation of its size. A larger or smaller A cation can cause the whole lattice to expand or contract and lead to change of the B–X bond length which has been demonstrated to be important in determination of bandgap.[87, 100]

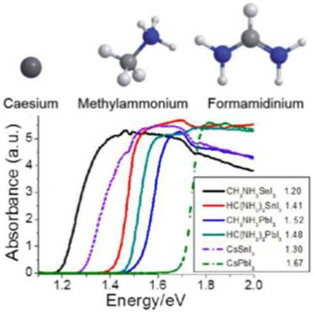

Figure 8. The atomic structure of the three A site cations in the discussion and the spectra of different perovskite prepared with the solution method as compared with $CsSnI_3$ and $CsPbI_3$ reference phases (dotted lines) prepared from the open tube method. The value of the band gap is given next to each compound. Reproduced from Ref. 101.

Given a particular metal and halide, for example $APbI_3$, relatively small size range is allowed for the A cation, since it must fit between the corner-sharing metal halide octahedral as indicated by the so-called tolerance factor (t). (*ut supra*) When t = 1, to maintain cubic symmetry, the value of ionic radius (R_A^+) may not be larger than 2.6 Å. If the caiton is too large, the 3D perovskite structure is unfavourable and lower-dimensional layered or confined perovskites will be formed.[102] An ethylammonium cation based perovskite has been explored previously in solar cells, and was shown to form a wider bandgap perovskite due to a 2H-type structure.[103] So far it has been proved that small monovalent cations, such as K^+, Rb^+, Cs^+, methylammonium (MA^+), or formanidinium (FA^+) can form three-dimensional (3D) framework with PbI_6 network.[19, 31, 104-110] Within the scope of this comparison, the effective ionic radius follow a trend of $R_{Cs}{}^+ < R_{MA}{}^+ < R_{FA}{}^+$ as illustrated in figure 8.[99] It is observed that $CsPbI_3$ absorbs up to a shorter wavelength, whereas $FAPbI_3$ absorbs to a longer wavelength than $MAPbI_3$. We can summarize that as the A cation increases in ionic radius, and hence the lattice would be expected to expand, the band gap decreases, causing a red-shift in the absorption onset. Enlightened by this phenomenon, Pellet et al. and Eperon et al. prepared formanidinium based perovskite and realized J_{SC} higher than 20 mA/cm^2.[42, 95] Also from figure 8, we have to note that when the metal is changed to a smaller Sn^{2+}, the trend in band gap is totally changed.

Influence of metal cation

There are numerous reports of Pb (II) and Sn (II) halide 3D perovskites, however only a few reports were made of the 3D perovskite family of $AGeX_3$ (A = Rb, Cs; X = Cl, Br, I).[23, 24, 111, 112] This is presumably because of the decreasing stability of the Ge(II) oxidation state when moving up the group on the periodic table. As was mentioned above, the X-M-X bond angle has been attributed to have the greatest impact on tuning the band gap for each individual metal. Taking AMI_3 (M = Ge, Sn, Pb) as an example, the M-I-M bridging angles between the MI_6 octahedra are 166.27(8)^o for Ge, 159.61(5)^o for Sn and 155.19(6)^o for Pb.[29] At the same time, with the downward selection of the metal cation, a decrease of the covalent character of M-I bond is observed, meaning the increase of the difference between the electron-negativity of the two atoms. Therefore the band gap of the group of perovskite follows the trend of $AGeI_3 < ASnI_3 < APbI_3$. It is obvious from figure 8 that all the Sn(II) based perovskites show lower band gap than that of Pb(II) based perovskites. Bearing this in mind, it is convenient to combine Sn halide perovskite with Pb perovskite to realize NIR absorbing perovskite solar cells. Although the edge of the IPCE curve reached 1060 nm, which was 260 nm red-shifted compared with that of $MAPbI_3$ perovskite solar cells, the efficiency was compromised by the disappointing Sn(II) stability.[96]

Influence of halide anion

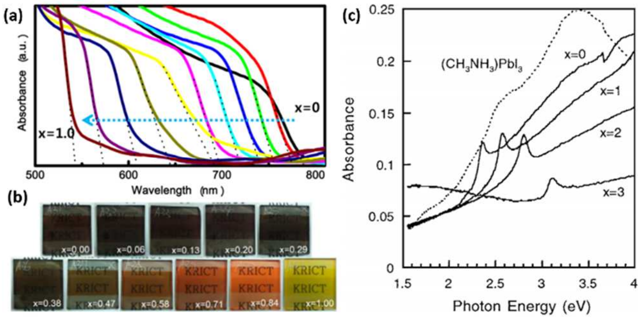

Figure 9. (a) UV−vis absorption spectra of FTO/c-TiO_2/m-TiO_2/$MAPb(I_{1-x}Br_x)_3$/Au cells measured using an integral sphere. (b) Photographs of 3D TiO_2/$MAPb(I_{1-x}Br_x)_3$ bilayer nanocomposites on FTO glass substrates. Reprinted with permission. [87] (c) Room temperature Visible-UV optical absorption spectra of the $MAPbI_3$ (dotted line) and the $MAPbBr_{3-x}Cl_x$ films (solid line). Reprinted with permission. [113]

Although people has observed an increase in lattice constants with the increasing atomic size of the anions from Cl to Br to I[114], electronic absorption spectra for Pb halide perovskite shift to longer wavelength by changing the halide from Cl to Br and I.[35, 36, 63, 87, 100, 25, 115, 116] In terms of further discussions purposes, we will limit ourselves to the $MAPbX_3$ systems where X = Cl, Br, and I, as the all the other 3D AMX_3 cases will follow the same trend. The natures of the CBM and VBM was studied by theoretical method and people found that the red shift of the bandgap as proceeding down the group (Cl ⟶ I) is due to the increase in covalent character of the halogen bonding with the lead, meaning a decrease of the electron-negativity of the halogen atom.[117] Interestingly, a perovskite structure which incorporates two halides (e.g. iodide with bromide[87, 95, 100] or bromide with chloride[113]) allows for the continuous tuning of the bandgap and the optical absorption to cover almost the entire visible spectrum. (Figure 9) On the other hand, however, no obvious band gap change was observed in the case of iodo-chloride mixed perovskite, indicating the mounting of Cl into the PbI_6 octahedron is very difficult.[40, 118]

Photovoltaic application of the perovskite materials

By virtue of the their ‘customizable’ low band gap, the perovskite absorbers showed superior advantages over traditional dyes by much more strongly absorbing over a broader range, enabling complete light absorption in films as thin as 500 nm. This is specifically favorable for the solid-state cells, where thickness limitations of around 2 μm have historically limited the light absorption and photocurrent generation.[119] And this time, lead(II)-based halide perovskites outperformed their tin(II) counterparts due to much smaller oxidation sensitivity and stronger photovoltage response.[101] So far only one report showed tin(II) perovskite ($MASnI_3$) was applied as light absorber in a solar cell[96] and another one with $CsSnI_3$ served as a p-type semiconductor (HTM) in a DSSC.[38] Due the extremely low PCE of oxide perovskite based solar cells, they will not be discussed in detail in this section.

Perovskite materials as light absorber with different composition

Triiodide

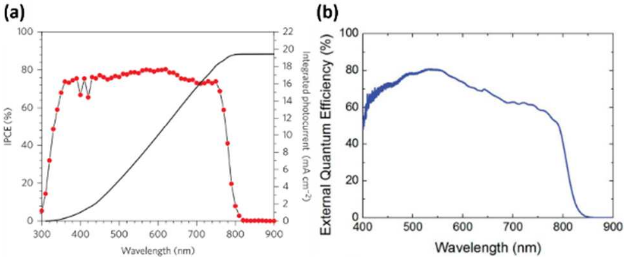

Figure 10. (a) IPCE spectrum of $MAPbI_3$ perovskite solar cell. The integrated product of the IPCE spectrum with the AM1.5G photon flux is also shown (black line). Reprinted with permission. [46]; (b) External quantum efficiency spectrum of a representative $FAPbI_3$ solar cell. Reproduced from Ref. 95.

The first record and certified solar cell obtained from organometal halide perovskite adopted methyl ammonium lead triiodide ($MAPbI_3$)[43, 46] as the light absorber and spiro-OMeTAD as HTM. (Figure 6b,e) $MAPbI_3$ as the most successfully applied perovskite material for light harvesting showed a narrow band gap of 1.55 eV[35], high extinction coefficient[36] and excellent incident-photon-to-current conversion efficiency (IPCE) in the solar cells[39, 120] until 800 nm, harvesting the photons from visible range to part of the near-infrared. (Figure 10a) Therefore, researchers realized ever growing PCEs in PV devices from 3.9%[35] to 15.7%[46] within four years. However, the short-circuit photocurrent density (J_{SC}) was limited to an average value of 17 mA/cm^2. In theory, a semiconductor with a band gap of 1.5 eV can deliver photocurrents up to 27 mA/cm^2 under standard AM1.5G illumination.

To achieve higher J_{SC}, people looked in to new pervskite materials with broader light harvesting ability based on the band gap engineering strategy discussed in the previous sections. Compared with $MAPbI_3$, formamidinium lead triiodide ($FAPbI_3$) shows a narrower band gap as 1.48 eV (~ 840nm absorption onset)[101], and hence lies even closer to that favorable for optimum solar conversion efficiencies.[42, 95, 121, 122] (Figure 10b) So far there was not much reports about devices based on $FAPbI_3$ and the highest PCE achieved is reported to be 14.2% by Eperon et al based on a planar heterojunction device structure. Although the average V_{OC} (0.85 V) and FF (60%) all dropped compared to those of $MAPbI_3$ and average efficiency is still below 10%, the average J_{SC} was increased to 18.8 mA/cm^2 and a record value of 23.3 mA/cm^2 was also reported.[95]

Partially replace the MA^+ in $MAPbI_3$ by FA^+ is an innovative way to make use of the advantages of both cations. Pellet et al demonstrated for the first time a perovskite-sensitized photovoltaic device based on the mixed cation perovskite $(MA)_x(FA)_{1-x}PbI_3$ (x = 0 to 1).[42] Here, the formamidinium (FA) cation is presented as a replacement for methylammonium (MA) in lead iodide perovskites. Devices based on pure $FAPbI_3$ were made via sequential deposition and gave PCE of 11.0% which is lower than that of $MAPbI_3$ due to the presence of the yellow δ-phase. Surprisingly, using the same deposition method and adding 20% MA into the FA dipping bath completely avoids the undesirable formation of the δ-phase while maintaining the red-shifted band gap of $FAPbI_3$. Moreover, the mixed-cation perovskite $MA_{0.6}FA_{0.4}PbI_3$ exhibits superior PV performance to the single cation analogues owing to a greater harvesting and collection of red photons resulting in higher average J_{SC} (19 mA/cm^2) without sacrificing photovoltage (~ 1 V) and FF (70%). This superior carrier collection efficiency is likely related to the longer exciton lifetime in the $MA_{0.6}FA_{0.4}PbI_3$ material exceeding 100 ns. Using this technique, it is possible to fabricate devices with average PCE of 13.4 % and record value up to 14.9 % under the AM1.5G simulated solar spectrum. (Figure 6a) The strategy of mixing organic ammonium cations opens up new possibilities of tuning the optical, electrical and morphological properties of the semiconducting sensitizers to further improve the photovoltaic efficiency of perovskite-sensitized solar cells.

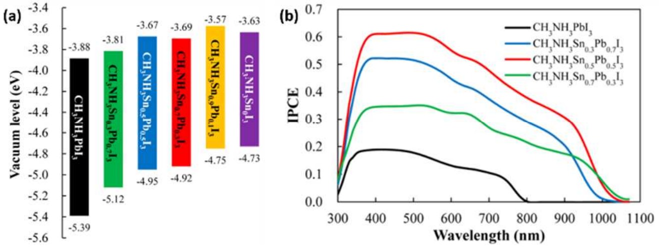

Figure 11. (a) Energy diagram for $CH_3NH_3Sn_xPb_{(1-x)}I_3$ perovskite; (b) IPCE curves for $CH_3NH_3Sn_xPb_{(1-x)}I_3$ perovskite/P3HT solar cells. Reprinted with permission. [96]

On the route to higher J_{SC}, replace the metal cation is an alternative method to narrow the band gap. In 1990 Yamada et al. showed for the first time structural phase transition and electrical conductivity of mixed-metal halide peovskite $MASn_{1-x}Pb_xBr_3$, while recently, Ogomi et al. reported photovoltaic performances of the first all solid-state Sn/Pb mixed perovskite solar cells.[96] It is interesting to note that pure Sn halide perovskite itself did not show photovoltaic properties until PbI_2 was added in SnI_2. The best performance was obtained by using $MASn_{0.5}Pb_{0.5}I_3$ perovskite and a 4.18% efficiency with open circuit voltage 0.42 V, fill factor 0.50, and short circuit current 20.04 mA/cm^2 were reported. Though the PCE of the device based on mixed-metal halide peovskite is quite ordinary, due to the fact that this new perovskite can harvest the light up to 1060 nm, it can be useful in a bottom cells for tandem perovskite solar cells. (Figure 11)

It is necessary to mention that besides spiro-OMeTAD, a broad variety of HTMs such as poly-(3-hexylthiophene-2,5-diyl) (P3HT), poly[*N*-9'-hepta-decanyl-2,7-carbazole-alt-5,5-(4',7'-di-2-thienyl-2',1',3'-benzothiadiazole)] (PCDTBT), PTAA, pyrene arylamine, CuI and CuSCN etc. have also been tested with interesting results.[81, 123-128]

Tribromide

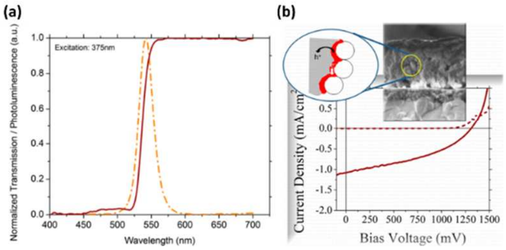

Figure 12. (a) Normalized transmission (solid line) and luminescence (dashed line) spectra of $MAPbBr_3$ film on glass. The luminescence was measured with 375 nm excitation; (b) J-V curve of solar cells with $MAPbBr_3$ as absorber and electron conductors on alumina scaffold. Reprinted with permission. [52]

Methyl ammonium lead tribromide ($MAPbBr_3$) was one of the earliest studied halide perovskite materials for solar cell absorber and has the reputation of giving higher V_{OC} compared to its triiodide counterparts due to its lower HOMO level, although the light harvesting ability is much weaker. (Figure 12a) After the first appearance in 2009 with a V_{OC} of 0.96 V, $MAPbBr_3$ has been used by several groups for solar cell absorber. First by Cai et al. and Noh et al., using conjugated polymers PCBTDPP or PTAA respectively as the HTM, the cells gave a high V_{OC} of 1.16 V[93] and 1.13 V[87]. Finally, Edri and co-workers reported that higher V_{OC} up to 1.3 V[52] can be obtained by using $MAPbBr_3$-coated alumina scaffold as absorber/electron conductors and PDI where HOMO level has lower energy in relation to the vacuum level as HTM. (Figure 12b) However, the PCE of these cells are very poor (< 4%) due to the short light absorption range and therefore low J_{SC}.

Mixed-halide perovskite

The first mixed halide perovskite $MAPbI_{3-x}Cl_x$ was developed by Snaith and coworkers and applied to a nonelectron injecting, mesoporous Al_2O_3 scaffold layer by spin-coating the mixture solution of MAI and $PbCl_2$ in 3:1 ratio, resulting in the so-called "meso-superstructured" solar cell.[40] (Equation 1) It is expected that the perovskite material $MAPbI_3$ and the byproduct MACl may form at the same time in the deposited thin film. However, according to XRD patterns, no sign of MACl exists inside the films and crystal of $MAPbI_3$ and $MAPbI_{3-x}Cl_x$ are identical. One hypothesis is that most of the excess organic MACl is sublimed leaving only traces Cl in the $MAPbI_3$ lattice. During the annealing procedure, the crystallization procession of perovskite is accompanied by this sublimation of MACl, which will have impact on the phase transformation control.[54, 65, 88, 90, 91] That is why the formula $MAPbI_{3-x}Cl_x$ is used to show the uncertainty of the Cl content.

$3MAI + PbCl_2 \rightarrow MAPbI_{3-x}Cl_x + 2MACl$ $(0 \leqslant x \leqslant 1)$ eq. 1

$MAPbI_{3-x}Cl_x$ can be seen as I^- ions in $MAPbI_3$ are partially substituted by Cl^- ion. The Cl^- doping will induce lattice distortion and the excess organic phase can prolong the crystallization procession. This is evidenced by the increased time necessary to fully anneal deposited films, specifically less than 1 h for pure iodine perovskite and between 2 to 3 h for the mixed halide perovskite. More significantly, this doping increases the environmental stability of the perovskite film[40] and the conductivity as well as charge diffusion length (~1 μm) of the perovskite domain without affecting its optical properties.[65, 118, 129] After the success in achieving a 11% PCE with $MAPbI_{3-x}Cl_x$ in a "meso-superstructured" solar cell, the trajectory of H. Snaith's team turned out to be twofold: firstly, they developed low-temperature processing routes for the m-Al_2O_3 scaffold[45, 47, 54] and compact TiO_2 layer[45, 47] to compatible with low cost fabrication on flexible organic substrate; secondly, in their following seminal reports, they aimed at further reducing complexity and ultimately returning to the very essentials of planar heterojunction solar cells by getting rid of the mesoporous scaffold without sacrificing efficiency.[44, 88, 130] Following these two tracks, fabulous J_{SC} (> 20 mA/cm), V_{OC} (> 1V) together with PCE (15.4% ~ 15.9%) values have been achieved and consolidated the position of organometal halide perovskite in the field of photovoltaic industry. (Figure 6c,d,f) (Table 1)

Mixed-halide perovskite $MAPb(I_{1-x}Br_x)_3$ $(0 \leqslant x \leqslant 1)$ has been made by either one step deposition[53, 87] or two-step sequential deposition process.[100] Although Noh claim that when x = 0.2 the stability of device (μ > 10%) was greatly improved, in contrast to the Cl^- ion doping in $MAPbI_3$, the inclusion of Br^- cannot bring much gain in the photovoltaic performance but rather the opposite effect with the increase of Br^- ratio. (Table 1)

The newest mixed-halide perovskite is $MAPbBr_{3-x}Cl_x$, which gave an extraordinarily high V_{OC} of 1.5 V. [94] Edri et al found that adding Cl to the $MAPbBr_3$ to yield $MAPbBr_{3-x}Cl_x$ improves the surface coverage and therefore increases the V_{OC}, FF, and, especially, the J_{SC}. Again, as is the case for the better-studied iodide analogue, no Cl is detected in the film by energy dispersive spectroscopy (EDS). (Table 1)

Versatility in fabrication techniques

Besides the excellent PV performance of the organometal halide perovskite, the title compound is also attractive because its versatility in fabrication techniques. So far there have been four different film deposition methods reported: one-step precursor solution deposition[39]; two-step sequential deposition[43]; dual-source vapor deposition[44] and vapor assisted solution procession.[131] All the first three methods have given efficiencies above 15% and been applied in fabricating perovskite solar cells on organic flexible substrate based on the low temperature processing technique.[46, 85, 91, 92, 132] (Table 1) (Figure 13) At the same time, methods to fabricate perovskite nanoparticle have been reported via template assisted[62] or template-free[133, 134] protocols.

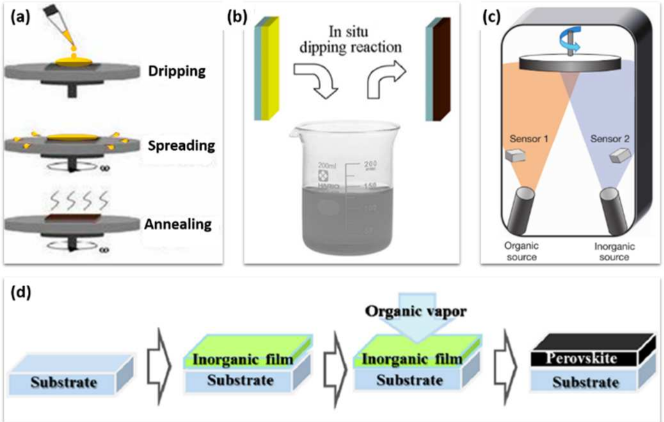

Figure 13. Four general methods to prepare perovskite active layers. (a) One-Step Precursor Deposition (OSPD); (b)

Sequential Deposition Method (SDM). Reprinted with permission. [122]; (c) Dual-Source Vapor Deposition (DSVD). Reprinted with permission. [44]; (d) Vapor-Assisted Solution Process (VASP) Reprinted with permission. [82]

One-Step Precursor Deposition (OSPD)

One-step precursor solution deposition represents the most popular thin film deposition method for perovskite solar cells due to its obvious simplicity.[35] (Figure 13a) Generally, the precursor solution of perovskite is prepared by mixing the powder of RAX (R: methyl, formamidine; X: I, Br) and PbX_2 (X: I, Br, Cl) at 1:1 (stoichiometry) or 3:1 (non-stoichiometry) mole ratio in high boiling point aprotic polar solvents (DMF, DMAc, DMSO, NMP, GBL etc.) at elevated temperature for several hour to get a clear solution. This solution is then used for the *in situ* formation of organometal halide perovskite by spin-casting or drop-casting[77] on a n-type contact layer. Normally, an annealing procession is needed for the complete transformation of precursor to perovskite crystalline film. After that a layer of HTM (e.g. spiro-OMeTAD) is deposited on top. With this fabrication technique several parameters could be tuned to further optimize the device performance e.g. thickness of c-TiO_2[47], thickness of m-TiO_2[36, 53, 67, 135] or m-Al_2O_3[54, 136], concentration of precursor solution[89], solvent type[89], thickness of the perovskite layer[88, 130], annealing temperature[137] and time as well as thickness of HTM layer[138]. So far the cell with the reported highest PCE record (15.9%) was achieved via one-step precursor solution deposition method. [47]

Sequential Deposition Method (SDM)

Two-step sequential deposition method (originally developed by Mitzi et al[139, 140]) was first used by Burschka et al. to fabricate perovskite thin film in a solar cell.[43] (Figure 13b) In a typical sequential deposition procedure, the PbI_2 is first spin-coated from solution in DMF onto the nanoporous titania film and subsequently transform into the perovskite by dipping into a solution of MAI in iso-propanol.[43] The perovskite formation is instantaneous within the nanoporous host upon contacting the two components. After annealing, spiro-OMeTAD as HTM was subsequently deposited by spin-coating. The two-step sequential procedure allows much better control over the perovskite morphology compared to the one-step deposition method by allowing better confinement of PbI_2 into the nanoporous network of TiO_2. Employing this technique for the fabrication of solid-state mesoscopic solar cells greatly improves the reproducibility of their performance, and allows achieving the first perovskite solar cell with a PCE of 15% and the highest PCE of a HTM free perovskite cell[79]. (Figure 6b) (Table 1) This finding opens up completely new opportunities for the fabrication of solution-processed photovoltaics with high power conversion efficiencies and stability that matches or even exceeds those of today's best thin film photovoltaic devices. With this ambition in mind, Pellet et al. fabricated highly efficient devices with a mixed-cation perovskite following the sequential deposition procedure.[42] At the same time, Liu et al made a planar heterojunction cell and realized a PCE of 15.7%, when he replaced the c-TiO_2 and m-TiO_2 layers by a single c-ZnO blocking layer but kept the rest steps almost the same as the Burschka's work.[46] (Figure 6e)

Dual-Source Vapor Deposition (DSVD)

Preparation of perovskite thin film under vacuum by vapor deposition procession was first reported by Salau[19] and then by Mitzi[141]. In 2013, Liu et al. modified the deposition condition and used a dual-source vapor deposition technique to prepare the thin film of mixed-halide perovskite as the absorbing layer in a planar heterojunction solar cell.[44] (Figure 13c) It was demonstrated that vapor-deposited perovskite films were extremely uniform with crystalline platelets at nanometer scale while solution-processed films only partially covered the substrate containing voids between the micrometer-sized crystalline platelets which extend directly to the compact TiO_2-coated FTO glass. The authors claimed that superior uniformity of the coated perovskite films without any pin-holes was the reason for the record efficiency of 15.4%. (Figure 6c) Later on, the same method was used by Henk and his colleagues to construct an inverted thin film solar cell with sublimated $MAPbI_3$ perovskite layer sandwiched between two very thin electron (polyTPD) and hole blocking layers (PCBM) consisting of organic molecules.[84] In this structure, which is typical for organic-photovoltaic and light-emitting devices, an organic transparent conductor (PEDOT:PSS) was used as the positive charge collecting contact. Remarkably, a high V_{OC} of 1.05 V and PCE of 12% were achieved, which together with the planar heterojunction device geometry indicated the possibility of applying it to flexible solar module.[85] (Table 1)

Vapor-Assisted Solution Process (VASP)

Yang and his colleagues reported a novel low-temperature approach for the deposition of perovskite absorbing layer called Vapor-Assisted Solution Process (VASP) which is like a combination of *SDM* and *DSVD*. [82] In this procession, PbI_2 films were deposited on fluorine-doped tin oxide (FTO) glass coated with a compact layer of TiO_2 (c-TiO_2), followed by annealing in MAI vapor at 150 °C in N_2 atmosphere for 2 h to form the perovskite films. (Figure 13d) The perovskite film derived from this approach exhibits full surface coverage, uniform grain structure with grain size up to micrometers, and 100% precursor transformation completeness. A film evolution study on perovskite transformation indicated an appropriate rearrangement of PbI_2 film during intercalation of MAI driven by the reduction of grain boundary energy. Facilitated by the excellent film quality, the $MAPbI_3$ materials enabled an impressive device PCE of 12.1% in a planar architecture.[82] VASP presents a simple, controllable, and versatile approach to the pursuit of high-quality perovskite film and the resulting high-performance PV devices. The author believed that by incorporating organic species into the as-deposited inorganic framework through vapor effectively avoids the high reaction rate of perovskite during co-deposition of precursors (OSPD) and concern about possible film deterioration when dipping an inorganic framework into an organic species solution (SDM).

Selective contacts

Perovskite solar cells (PSCs) exhibit some differences with their most immediate predecessors, the dye-sensitized solar cells (DSSCs). For example, similar PCEs have been achieved in devices employing mesoporous TiO_2, nanostructured Al_2O_3 (ZrO_2), or even no mesoporous scaffold at all;[40, 43, 44, 80, 83] while DSSCs cannot perform well without using a conductive and mesoporous scaffold to deposit the sensitizer and collect the photocurrent.[142] On the other hand, cells with significant efficiency have been produced with even no hole-transporting media.[55, 78, 79] All these different functioning device geometries highlight the importance of understanding the effect of selective contacts in efficient charge separation.[143, 144] (Table 2)

Table 2. Selective contacts in a perovskite solar cell (PSC) with different devices geometry

Device geometry	Substrate	Electron-selective contact	Scaffold	Hole-selective contact
Mesoporous N-type oxide based PSCs	FTO glass	Compact TiO_2	Meso-TiO_2	Spiro-OMeTAD

				Other small molecules
				Polymers
				Inorganic molecules
Inert oxide based Meso-superstructured PSCs	FTO glass	Compact TiO_2	Meso-Al_2O_3	Spiro-OMeTAD
			Meso-ZrO_2	
Mesoporous P-type oxide based PSCs		N/A	N/A	NiO
Planar heterojunction-structured PSCs	FTO or ITO glass	Compact TiO_2	no	Spiro-OMeTAD
		Graphene/TiO_2 Nanocomposites	no	
		Compact ZnO_2	no	
Hybrid perovskite solar cells (inverted)	FTO or ITO glass	C60/PCBM	no	Polymers or PEDOT:PSS
Flexible perovskite solar cells.	PET/ITO/ZnO	PCBM	no	PEDOT:PSS

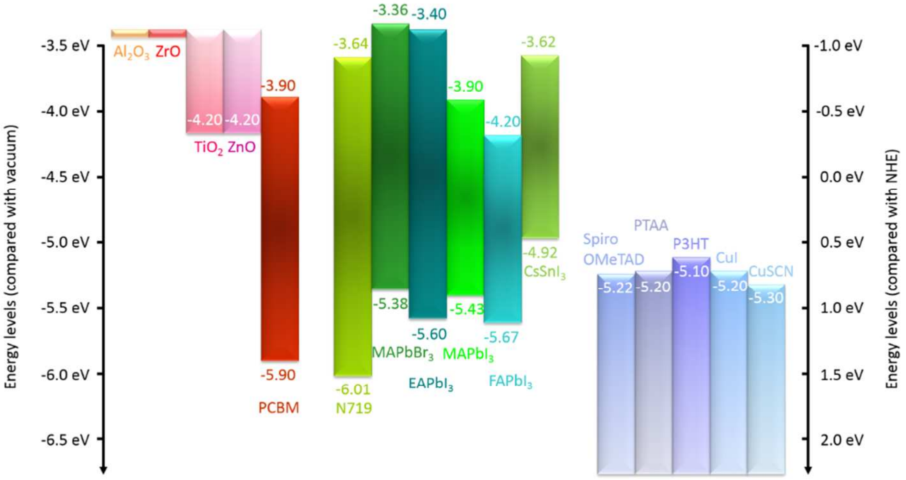

Figure 14. Schematic of literature values for energy level alignment for different materials acting as electron selective contact material (ETM) (left), absorbers (middle) and hole selective contact materials (HTM) (right) in solar cells. It is very probable that at least some of these levels change, if brought into contact with each other. The band gaps and, even more important, band edge positions, reported in the literature are spread over a wide range.

Different from sensitizers used in a DSSC, perovskite itself can accumulate charge,[145] a property which will have significant influence on the final device structure. In a typical PSCs, the most commonly used selective contact materials for electrons and holes are compact TiO_2 and spiro-OMeTAD, respectively.[146, 147] Nevertheless, finding another selective hole contact is one of the hottest branch topics about PSCs. Different low HOMO molecules[52, 69, 124, 126, 148] and polymers[81, 93, 123, 127] and also inorganic CuI[125] and CuSCN[128] have been used as hole-selective contacts and some of them showed comparable performance to that of spiro-OMeTAD. In contrast, a much smaller variety of materials has been checked as an alternative electron-selective contact: C_{60}/PCBM,[84, 149] graphene/TiO_2 nanocomposites,[45] nanocrystalline anatase[40]/rutile TiO_2[83] and ZnO[46] are some of the few examples. More recent reports[91] also described so-called inverted cell structure (light first passes through the hole selective contact instead of the electron selective contact) with a perovskite layer sandwiched between PCBM and PEDOT:PSS and PSC on flexible substrate with low temperature processed ZnO electron selective contact.[150] For the same purpose, Yella et al. also demonstrated low temperature deposition of a nanocrystalline TiO_2 (rutile) hole-blocking layer on a FTO conducting glass substrate via hydrolysis of $TiCl_4$ at 70°C, forming the electron selective contact with the photoactive $MAPbI_3$ film.[83] A collection of energy level alignments for different materials commonly used in PSC are show in figure 14.

Juárez-Pérez et al, has studied the role of the selective contacts in PSCs by impedance spectroscopy (IS) and found that three major roles played by it: transport resistance at the selector layer, charge-transfer rate at the interface (that could affect the bulk carrier density and consequently bulk recombination), and the surface recombination at the selective contact interface. It has been found that the nature of both electrons and holes selective contacts contribute to enhancement of the cell FF, while the hole-selective contact is mainly responsible for the high V_{OC}.[151] For example, judiciously selected combination of inert scaffold with perovskites and low HOMO HTM, e.g. $ZrO_2/MAPbI_3$/spiro-OMeTAD[80], $Al_2O_3/MAPbBr_3$/*N*,*N'*-dialkylperylenediimide (PDI)[52] and $Al_2O_3/MAPbBr_{3-x}Cl_x$/4,4'-bis(*N*-carbazolyl)-1,1'-biphenyl (CBP)[94] showed record V_{OC}s renewing continuously from 1.07 V to 1.3 V and finally 1.5 V. (Table 1)

PV dynamics and mechanism study

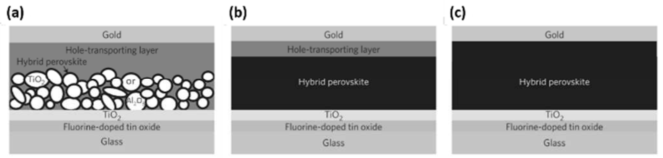

Figure 15. Architectures of perovskite solar cells. (a) Hybrid perovskite solar cell on mesoporous metal oxide; (b) Planar hybrid perovskite solar cell; (c) Heterojunction perovskite solar cell.

The performance of organometallic perovskite solar cells has rapidly surpassed that of both conventional dye-sensitized and organic photovoltaics. However, the understanding of the mechanisms underlying such exceptional performance has not grown at the same pace. Due to the fact that high power conversion efficiency can be realized in both mesoporous and thin-film device architectures, controversies exist and questions are open on a series of topics: the necessity of n-type meso-porous layer (is electron injection necessary?); sensitized or a heterojunction solar cell; low exciton binding energy (30 - 50 mV) (selective contact device?); the role of the HTM layer (direct contact between Au and perovskite) etc. (Figure 15) Focusing on the two necessary and successive processes for photovoltaic conversions: accumulation of a photogenerated charge and charge separation,[143] much effort is under way to characterize these different processes occurring in the perovskite layer measuring the diffusion length (L_D) in *ad hoc* prepared samples[64, 65] or complete devices[145, 152] and the lifetime.[123, 153, 154]

It is known that organometal halide perovskites work both as absorber and ambipolar charge transporter.[155] So to find out the necessity of n-type mesoporous layer, Moser and his colleagues used time-resolved techniques to study the kinetics of interfacial electron transfer processes of $MAPbI_3$ film on TiO_2 and Al_2O_3. Using ultrafast spectroscopy in the near-infrared, they were able to monitor transient absorption by photogenerated charges in the perovskite. Primary charge separation occurs at both selective contacts, with TiO_2 and the hole-transporting material, simultaneously, with ultrafast electron and hole injection taking place from the photoexcited perovskite over similar timescales. However, charge recombination is shown to be significantly slower on TiO_2 than on Al_2O_3 films.

Snaith and colleagues[65] and Nripan Mathew with collaborators[64] independently reported on diffusion-length measurements performed on hybrid perovskites, which shed light on the dynamics of photoexcited species (excitons or charge carriers) in these materials. Both teams used photoluminescence quenching experiments to measure the electron–hole diffusion length. They deposited on top of a perovskite thin-film a layer of quenching molecules, which act as a sink for the photoexcited species that, travelling in the film, reach the interface between the perovskite and the quencher. The photoluminescence dynamics of the material under study are therefore dependent on the thickness of the thin film and on the L_D of the photoexcitations, the latter of which can be extracted by modelling the photoluminescence decay curves according to a simple one-dimensional diffusion equation. Both teams obtain L_D of about 100 nm for electrons and holes in $MAPbI_3$. Furthermore, the group of Snaith also investigated the mixed-halide perovskite $MAPbI_{3-x}Cl_x$, obtaining in this case a L_D exceeding 1 μm. This high value reinforces hope for the future of hybrid perovskite solar cells, because it makes possible the fabrication of devices with thicker active layers, where the absorption of light can be increased without affecting the collection efficiency of the generated charges. Edri et al further developed this observation by studying electron beam-induced current (EBIC) imaging of cross sections of flat cells based on $MAPbI_3$ and $MAPbI_{3-x}Cl_x$ respectively and found that the L_D of electrons is shorter than that of holes ($L_{eff,\,e^-}/L_{eff,\,h^+} < 1$) in $MAPbI_3$, with the latter being at least 1 μm. They believe that this could explain why $MAPbI_3$-based cells require mesoporous electron-selective contact, while $MAPbI_{3-x}Cl_x$ ones, where L_D values are comparable for both charge types, do not.

On the other hand, impedance spectroscopy measurements were carried out to study the transport coupled with recombination process in perovskite solar cells.[152] Gonzalez-Pedro et al. found that a large diffusion length is achieved in compact film of $MAPbI_{3-x}Cl_x$, while the metal oxide nanostructure increases the L_D of $MAPbI_3$ perovskite. For the first time, they reported the measurement of the diffusion length in a nanostructured perovskite solar cell. Their model and conclusion are in good agreement with the above mentioned results for thin film $MAPbI_{3-x}Cl_x$ measured by Snaith et al. and Edri et al. but with a completely different technique.

The necessity of hole-selective contact was also studied by fabricating depleted hole conductor free $MAPbI_3/TiO_2/Au$ solar cells. Etgar et al.[78] performed capacitance voltage measurements and observed the self-doping density of the $MAPbI_3$ as well as the depletion layer which extends to both sides, the mesoporous TiO_2 film and the $MAPbI_3$ layer. The built-in field of the depletion region assists in the charge separation and suppresses the back recombination of electrons from the TiO_2 film to the $MAPbI_3$ film. Meanwhile, Shi et al.[79] observed a linear relationship between J_{SC} and light intensity in a similar cell, which means that carriers can transport smoothly in the semiconductors and there is no obvious difference in the transport velocity between electrons and holes.[156-158] It is in agreement with the above mentioned results of carrier diffusion constants of $MAPbI_3$ by Snaith et al and previous experimental results in the literature.[39] The above analyses reveal that $TiO_2/MAPbI_3/Au$ is a typical heterojunction solar cell, in which the n-type wide-band-gap TiO_2 acts as a window layer, and the $MAPbI_3$ acts as an absorber layer.

Conclusions and outlook

This minireview has unraveled an underexplored eclectic class of materials, hybrid oxide/halide perovskites, following the timeline and highlighted the state-of-the-art for its application in solar cells from the perspectives of material science and device engineering. The utilization of these hybrid perovskites offers both the advantages of the organic compounds, such as solution processability and optical properties tunability, and those of the inorganic crystalline semiconductors, like high charge mobilities and large absorption coefficients. It is not often that such a 'dirty cheap' and easily available material can perform all the three basic tasks required in solar cells operation, that is, light absorption, carrier generation, and ambipolar transport. The unique combination of all these advantages has signified a field breakthrough during last two years, allowing novel device layouts leading to record performances from just a few percent in a forerunner of perovskite cells to more than 16%, leaving the conventional dye-sensitized and organic photovoltaics far behind and holding the promise of cost effective solar energy production.

In addition to further optimizing the morphology of the known perovskite absorber (thickness and homogeneousity) and finding an even better HTM with higher mobility and HOMO of over 5 eV, one can also looking in to the possibility of atomistic modification of the perovskite. Hybrid perovskites have been shown to exhibit spontaneous electric polarization, which can be tuned through judicious choice of the organic cations with different dipole moment (e.g. $NH_3CH_3 < NH_3CH_3F < NH_3CHF_2 < NH_3CF_3$).[159] The presence of ferroelectric domains will result in internal junctions that may aid separation of photoexcited electron and hole pairs, and reduction of recombination through segregation of charge carriers. Studies have shown that when the perovskite is introduced into a TiO_2 mesoporous structure, electron injection from perovskite to the metal oxide is efficient in less than a picosecond but the lower intrinsic electron mobility of TiO_2 leads to unbalanced charge transport.[160] Therefore finding a metal oxide with higher electron mobility and fermi level may further increase the performance of this class of solar cells. In the case of $MAPbI_3$ perovskite with a band gap of 1.57 eV (corresponding to an onset of light absorption is ca. 790 nm), a short circuit current density (J_{SC}) of 28 mA/cm^2 is theoretically achievable. To date, V_{OC}, FF and J_{SC} values of 1.1 V, 0.7 and 21 mA/cm^2, respectively, have already been achieved. If we take into account the perovskite film absorption in the range 400–800 nm and 85 % of IPCE is achievable, a short circuit current of 24 mA/cm^2 is thermodynamically achievable and with FF of 0.8, the power conversion efficiency could be as high as 21%. Realizing 0.8 FF is possible by suppressing effectively the recombination by engineering the selective contacts and optimizing doping of the HTM.

One drawback of perovskite-based solar cells is the use of lead, which in combination with another weak point - water sensitivity will undermine the credit earned by the excellent PV performance. Therefore there is a drive to replace Pb^{2+} with a less toxic element such as Sn^{2+}, Cu^{2+} or Fe^{2+} as one of the obvious candidates or completely move on to perovskite oxide derivatives. Considering the oxygen sensitivity of Sn^{2+} and Fe^{2+}, perovskite oxide may be a better option. As a promising representative, a doped ferroelectrics $BaNi_{1/2}Nb_{1/2}O_{3-\delta}$□(BNNO) with a band gap as low as 1.1 eV has already been reported. Ab-initio calculations are needed as guidance to identify newer families of photovoltaic perovskites.

Similar to other relatively young photovoltaic technologies, perovskite solar cells can be fashioned using common wet chemistry techniques. The simplicity of making solar-cell components via liquid-phase chemical reactions and depositing the materials by methods such as spraying, screen-printing and ink-jet printing may make it possible for solar-cell manufacturers to eventually replace clean rooms and sophisticated manufacturing equipment with simple bench top processes. The fast-paced improvement, which hasn't shown signs of slowing, coupled with inexpensive materials and preparation methods, prompts a new paradigm. It will not be an exaggeration that one day perovskite based solar cells can match the capability and capacity of its arch rival silicon and power our planet.

Acknowledgements

The authors acknowledge funding from the European Union Seventh Framework Programme [FP7/2007-2013] under grant agreement n° 604032 of the MESO project, 309194 of the GLOBASOL project and 308997 of the NANOMATCELL project. MKN thank the Center of Excellence for Advanced Materials Research (CEAMR), King Abdulaziz University, Jeddah, Saudi Arabia for distinguished Adjunct Professor program.

Notes and references

Laboratory for Photonics and Interfaces, Institution of Chemical Sciences and Engineering, School of Basic Sciences, Swiss Federal Institute of Technology, CH-1015 Lausanne, Switzerland. E-mail: peng.gao@epfl.ch, mdkhaja.nazeeruddin@epfl.ch

1. M. D. Graef and M. McHenry, *Structure of materials: an introduction to crystallography, diffraction and symmetry*, Cambridge University Press, 2007.
2. D. B. Mitzi, *Journal of the Chemical Society-Dalton Transactions*, 2001, 1-12.
3. A. G. Chynoweth, *Physical Review*, 1956, **102**, 705-714.
4. Z. Y. Cheng, S. H. Liu, P. W. Beines, N. Ding, P. Jakubowicz and W. Knoll, *Chem. Mater.*, 2008, **20**, 7215-7219.
5. F. S. Chen, *J. Appl. Phys.*, 1969, **40**, 3389-&.
6. T. Choi, S. Lee, Y. J. Choi, V. Kiryukhin and S. W. Cheong, *Science*, 2009, **324**, 63-66.
7. S. Y. Yang, J. Seidel, S. J. Byrnes, P. Shafer, C. H. Yang, M. D. Rossell, P. Yu, Y. H. Chu, J. F. Scott, J. W. Ager, 3rd, L. W. Martin and R. Ramesh, *Nat. Nanotechnol.*, 2010, **5**, 143-147.
8. D. Cao, C. Wang, F. Zheng, W. Dong, L. Fang and M. Shen, *Nano Lett.*, 2012, **12**, 2803-2809.
9. M. Alexe and D. Hesse, *Nature Communications*, 2011, **2**.
10. M. Qin, K. Yao and Y. C. Liang, *Appl. Phys. Lett.*, 2008, **93**, -.
11. W. S. Choi, M. F. Chisholm, D. J. Singh, T. Choi, G. E. Jellison, Jr. and H. N. Lee, *Nat Commun*, 2012, **3**, 689.
12. J. Kreisel, M. Alexe and P. A. Thomas, *Nat. Mater.*, 2012, **11**, 260.
13. V. M. Fridkin, *Photoferroelectrics*, Springer, 1979.
14. Y. Inoue, K. Sato, K. Sato and H. Miyama, *J. Phys. Chem.*, 1986, **90**, 2809-2810.
15. S. M. Young and A. M. Rappe, *Phys. Rev. Lett.*, 2012, **109**, 116601.
16. S. M. Young, F. Zheng and A. M. Rappe, *Phys. Rev. Lett.*, 2012, **109**, 236601.
17. A. M. Glass, D. V. D. Linde and T. J. Negran, *Appl. Phys. Lett.*, 1974, **25**, 233-235.
18. I. Grinberg, D. V. West, M. Torres, G. Gou, D. M. Stein, L. Wu, G. Chen, E. M. Gallo, A. R. Akbashev, P. K. Davies, J. E. Spanier and A. M. Rappe, *Nature*, 2013, **503**, 509-512.
19. A. M. Salau, *Solar Energy Materials*, 1980, **2**, 327-332.
20. M. Schoijet, *Solar Energy Materials*, 1979, **1**, 43-57.
21. Netherco.Ah, *Phys. Rev. Lett.*, 1974, **33**, 1088-1091.
22. T. Ishihara, J. Takahashi and T. Goto, *Solid State Commun.*, 1989, **69**, 933-936.
23. D. B. Mitzi, *Chem. Mater.*, 1996, **8**, 791-800.
24. G. C. Papavassiliou and I. B. Koutselas, *Synth. Met.*, 1995, **71**, 1713-1714.
25. J. Calabrese, N. L. Jones, R. L. Harlow, N. Herron, D. L. Thorn and Y. Wang, *J. Am. Chem. Soc.*, 1991, **113**, 2328-2330.
26. D. B. Mitzi, C. A. Feild, W. T. A. Harrison and A. M. Guloy, *Nature*, 1994, **369**, 467-469.
27. D. B. Mitzi, S. Wang, C. A. Feild, C. A. Chess and A. M. Guloy, *Science*, 1995, **267**, 1473-1476.
28. D. B. Mitzi, *Journal of the Chemical Society, Dalton Transactions*, 2001, 1-12.
29. J. L. Knutson, J. D. Martin and D. B. Mitzi, *Inorg. Chem.*, 2005, **44**, 4699-4705.
30. Y. H. Chang, C. H. Park and K. Matsuishi, *Journal of the Korean Physical Society*, 2004, **44**, 889-893.
31. C. K. Moller, *Nature*, 1957, **180**, 981-982.

32. C. K. Moller, *Nature*, 1958, **182**, 1436-1436.
33. J. H. Burroughes, D. D. C. Bradley, A. R. Brown, R. N. Marks, K. Mackay, R. H. Friend, P. L. Burns and A. B. Holmes, *Nature*, 1990, **347**, 539-541.
34. C. R. Kagan, D. B. Mitzi and C. D. Dimitrakopoulos, *Science*, 1999, **286**, 945-947.
35. A. Kojima, K. Teshima, Y. Shirai and T. Miyasaka, *J. Am. Chem. Soc.*, 2009, **131**, 6050-6051.
36. J. H. Im, C. R. Lee, J. W. Lee, S. W. Park and N. G. Park, *Nanoscale*, 2011, **3**, 4088-4093.
37. J. Burschka, A. Dualeh, F. Kessler, E. Baranoff, N. L. Cevey-Ha, C. Yi, M. K. Nazeeruddin and M. Gratzel, *J. Am. Chem. Soc.*, 2011, **133**, 18042-18045.
38. I. Chung, B. Lee, J. He, R. P. Chang and M. G. Kanatzidis, *Nature*, 2012, **485**, 486-489.
39. H. S. Kim, C. R. Lee, J. H. Im, K. B. Lee, T. Moehl, A. Marchioro, S. J. Moon, R. Humphry-Baker, J. H. Yum, J. E. Moser, M. Gratzel and N. G. Park, *Sci Rep*, 2012, **2**, 591.
40. M. M. Lee, J. Teuscher, T. Miyasaka, T. N. Murakami and H. J. Snaith, *Science*, 2012, **338**, 643-647.
41. U. Bach, D. Lupo, P. Comte, J. E. Moser, F. Weissortel, J. Salbeck, H. Spreitzer and M. Gratzel, *Nature*, 1998, **395**, 583-585.
42. N. Pellet, P. Gao, G. Gregori, T. Y. Yang, M. K. Nazeeruddin, J. Maier and M. Gratzel, *Angew Chem Int Ed Engl*, 2014, **53**, 3151-3157.
43. J. Burschka, N. Pellet, S. J. Moon, R. Humphry-Baker, P. Gao, M. K. Nazeeruddin and M. Gratzel, *Nature*, 2013, **499**, 316-319.
44. M. Liu, M. B. Johnston and H. J. Snaith, *Nature*, 2013, **501**, 395-398.
45. J. T. Wang, J. M. Ball, E. M. Barea, A. Abate, J. A. Alexander-Webber, J. Huang, M. Saliba, I. Mora-Sero, J. Bisquert, H. J. Snaith and R. J. Nicholas, *Nano Lett.*, 2014, **14**, 724-730.
46. D. Liu and T. L. Kelly, *Nat. Photonics*, 2013, **8**, 133-138.
47. K. Wojciechowski, M. Saliba, T. Leijtens, A. Abate and H. J. Snaith, *Energy & Environmental Science*, 2014, **7**, 1142.
48. M. A. Green, K. Emery, Y. Hishikawa, W. Warta and E. D. Dunlop, *Progress in Photovoltaics*, 2013, **21**, 827-837.
49. "http://www.nrel.gov/ncpv/images/efficiency_chart.jpg", The National Renewable Energy Laboratory (NREL) 2013.
50. M. He, D. Zheng, M. Wang, C. Lin and Z. Lin, *Journal of Materials Chemistry A*, 2014.
51. S. Dharani, H. K. Mulmudi, N. Yantara, P. T. Thu Trang, N. G. Park, M. Graetzel, S. Mhaisalkar, N. Mathews and P. P. Boix, *Nanoscale*, 2014, **6**, 1675-1679.
52. E. Edri, S. Kirmayer, D. Cahen and G. Hodes, *The Journal of Physical Chemistry Letters*, 2013, **4**, 897-902.
53. J. Qiu, Y. Qiu, K. Yan, M. Zhong, C. Mu, H. Yan and S. Yang, *Nanoscale*, 2013, **5**, 3245-3248.
54. J. M. Ball, M. M. Lee, A. Hey and H. J. Snaith, *Energy & Environmental Science*, 2013, **6**, 1739-1743.
55. L. Etgar, P. Gao, Z. Xue, Q. Peng, A. K. Chandiran, B. Liu, M. K. Nazeeruddin and M. Gratzel, *J. Am. Chem. Soc.*, 2012, **134**, 17396-17399.
56. T. Ishihara, *J. Lumin.*, 1994, **60-1**, 269-274.
57. Z. Y. Cheng and J. Lin, *CrystEngComm*, 2010, **12**, 2646-2662.
58. P. Mauersberger and F. Huber, *Acta Crystallographica Section B-Structural Science*, 1980, **36**, 683-684.
59. K. Shum, Z. Chen, J. Qureshi, C. L. Yu, J. J. Wang, W. Pfenninger, N. Vockic, J. Midgley and J. T. Kenney, *Appl. Phys. Lett.*, 2010, **96**.
60. D. B. Mitzi, K. Chondroudis and C. R. Kagan, *Inorg. Chem.*, 1999, **38**, 6246-6256.
61. P. K. Nayak, G. Garcia-Belmonte, A. Kahn, J. Bisquert and D. Cahen, *Energy & Environmental Science*, 2012, **5**, 6022-6039.
62. A. Kojima, M. Ikegami, K. Teshima and T. Miyasaka, *Chem. Lett.*, 2012, **41**, 397-399.
63. K. Tanaka, T. Takahashi, T. Ban, T. Kondo, K. Uchida and N. Miura, *Solid State Commun.*, 2003, **127**, 619-623.
64. G. Xing, N. Mathews, S. Sun, S. S. Lim, Y. M. Lam, M. Gratzel, S. Mhaisalkar and T. C. Sum, *Science*, 2013, **342**, 344-347.
65. S. D. Stranks, G. E. Eperon, G. Grancini, C. Menelaou, M. J. Alcocer, T. Leijtens, L. M. Herz, A. Petrozza and H. J. Snaith, *Science*, 2013, **342**, 341-344.
66. A. Marchioro, J. Teuscher, D. Friedrich, M. Kunst, R. van de Krol, T. Moehl, M. Grätzel and J.-E. Moser, *Nat. Photonics*, 2014, **8**, 250-255.
67. A. Dualeh, T. Moehl, N. Tetreault, J. Teuscher, P. Gao, M. K. Nazeeruddin and M. Gratzel, *ACS Nano*, 2014, **8**, 362-373.
68. R. Lindblad, D. Bi, B.-w. Park, J. Oscarsson, M. Gorgoi, H. Siegbahn, M. Odelius, E. M. J. Johansson and H. Rensmo, *The Journal of Physical Chemistry Letters*, 2014, **5**, 648-653.
69. E. Edri, S. Kirmayer, A. Henning, S. Mukhopadhyay, K. Gartsman, Y. Rosenwaks, G. Hodes and D. Cahen, *Nano Lett.*, 2014, **14**, 1000-1004.
70. W. Shockley and H. J. Queisser, *J. Appl. Phys.*, 1961, **32**, 510-&.
71. Y. Takeoka, K. Asai, M. Rikukawa and K. Sanui, *Bull. Chem. Soc. Jpn.*, 2006, **79**, 1607-1613.
72. H. W. Eng, P. W. Barnes, B. M. Auer and P. M. Woodward, *J. Solid State Chem.*, 2003, **175**, 94-109.
73. J. Etourneau, J. Portier and F. Menil, *J. Alloys Compd.*, 1992, **188**, 1-7.
74. M. Jansen and H. P. Letschert, *Nature*, 2000, **404**, 980-982.
75. E. Knittle and R. Jeanloz, *Science*, 1987, **235**, 668-670.
76. R. Marchand, F. Tessier, A. Le Sauze and N. Diot, *International Journal of Inorganic Materials*, 2001, **3**, 1143-1146.
77. Z. Ku, Y. Rong, M. Xu, T. Liu and H. Han, *Sci Rep*, 2013, **3**, 3132.
78. W. A. Laban and L. Etgar, *Energy & Environmental Science*, 2013, **6**, 3249.
79. J. Shi, J. Dong, S. Lv, Y. Xu, L. Zhu, J. Xiao, X. Xu, H. Wu, D. Li, Y. Luo and Q. Meng, *Appl. Phys. Lett.*, 2014, **104**, 063901.
80. D. Q. Bi, S. J. Moon, L. Haggman, G. Boschloo, L. Yang, E. M. J. Johansson, M. K. Nazeeruddin, M. Gratzel and A. Hagfeldt, *Rsc Advances*, 2013, **3**, 18762-18766.
81. J. H. Heo, S. H. Im, J. H. Noh, T. N. Mandal, C.-S. Lim, J. A. Chang, Y. H. Lee, H.-j. Kim, A. Sarkar, M. K. Nazeeruddin, M. Grätzel and S. I. Seok, *Nat. Photonics*, 2013, **7**, 486-491.
82. Q. Chen, H. Zhou, Z. Hong, S. Luo, H. S. Duan, H. H. Wang, Y. Liu, G. Li and Y. Yang, *J. Am. Chem. Soc.*, 2014, **136**, 622-625.
83. A. Yella, L. P. Heiniger, P. Gao, M. K. Nazeeruddin and M. Gratzel, *Nano Lett.*, 2014.
84. O. Malinkiewicz, A. Yella, Y. H. Lee, G. M. Espallargas, M. Graetzel, M. K. Nazeeruddin and H. J. Bolink, *Nat. Photonics*, 2013, **8**, 128-132.

85. C. Roldán-Carmona, O. Malinkiewicz, A. Soriano, G. Mínguez Espallargas, A. Garcia, P. Reinecke, T. Kroyer, M. I. Dar, M. K. Nazeeruddin and H. J. Bolink, *Energy & Environmental Science*, 2014, **7**, 994.
86. S. Y. Sun, T. Salim, N. Mathews, M. Duchamp, C. Boothroyd, G. C. Xing, T. C. Sum and Y. M. Lam, *Energy & Environmental Science*, 2014, **7**, 399-407.
87. J. H. Noh, S. H. Im, J. H. Heo, T. N. Mandal and S. I. Seok, *Nano Lett.*, 2013, **13**, 1764-1769.
88. G. E. Eperon, V. M. Burlakov, P. Docampo, A. Goriely and H. J. Snaith, *Adv. Funct. Mater.*, 2014, **24**, 151-157.
89. B. Conings, L. Baeten, C. De Dobbelaere, J. D'Haen, J. Manca and H. G. Boyen, *Adv Mater*, 2013, n/a-n/a.
90. A. Abrusci, S. D. Stranks, P. Docampo, H. L. Yip, A. K. Jen and H. J. Snaith, *Nano Lett.*, 2013, **13**, 3124-3128.
91. P. Docampo, J. M. Ball, M. Darwich, G. E. Eperon and H. J. Snaith, *Nat Commun*, 2013, **4**, 2761.
92. J. You, Z. Hong, Y. M. Yang, Q. Chen, M. Cai, T. B. Song, C. C. Chen, S. Lu, Y. Liu, H. Zhou and Y. Yang, *ACS Nano*, 2014, **8**, 1674-1680.
93. B. Cai, Y. D. Xing, Z. Yang, W. H. Zhang and J. S. Qiu, *Energy & Environmental Science*, 2013, **6**, 1480-1485.
94. E. Edri, S. Kirmayer, M. Kulbak, G. Hodes and D. Cahen, *Journal of Physical Chemistry Letters*, 2014, **5**, 429-433.
95. G. E. Eperon, S. D. Stranks, C. Menelaou, M. B. Johnston, L. M. Herz and H. J. Snaith, *Energy & Environmental Science*, 2014, **7**, 982.
96. Y. Ogomi, A. Morita, S. Tsukamoto, T. Saitho, N. Fujikawa, Q. Shen, T. Toyoda, K. Yoshino, S. S. Pandey, T. Ma and S. Hayase, *The Journal of Physical Chemistry Letters*, 2014, **5**, 1004-1011.
97. S. R. Basu, L. W. Martin, Y. H. Chu, M. Gajek, R. Ramesh, R. C. Rai, X. Xu and J. L. Musfeldt, *Appl. Phys. Lett.*, 2008, **92**.
98. S. Y. Yang, L. W. Martin, S. J. Byrnes, T. E. Conry, S. R. Basu, D. Paran, L. Reichertz, J. Ihlefeld, C. Adamo, A. Melville, Y. H. Chu, C. H. Yang, J. L. Musfeldt, D. G. Schlom, J. W. Ager and R. Ramesh, *Appl. Phys. Lett.*, 2009, **95**.
99. I. Borriello, G. Cantele and D. Ninno, *Physical Review B*, 2008, **77**.
100. S. A. Kulkarni, T. Baikie, P. P. Boix, N. Yantara, N. Mathews and S. G. Mhaisalkar, *Journal of Materials Chemistry A*, 2014.
101. C. C. Stoumpos, C. D. Malliakas and M. G. Kanatzidis, *Inorg. Chem.*, 2013, **52**, 9019-9038.
102. D. B. Mitzi, *Progress in Inorganic Chemistry, Vol 48*, 1999, **48**, 1-121.
103. J. H. Im, J. Chung, S. J. Kim and N. G. Park, *Nanoscale Res Lett*, 2012, **7**, 353.
104. D. Weber, *Zeitschrift Fur Naturforschung Section B-a Journal of Chemical Sciences*, 1978, **33**, 862-865.
105. D. Weber, *Zeitschrift Fur Naturforschung Section B-a Journal of Chemical Sciences*, 1978, **33**, 1443-1445.
106. K. Yamada, T. Tsuritani, T. Okuda and S. Ichiba, *Chem. Lett.*, 1989, 1325-1328.
107. K. Yamada, S. Funabiki, H. Horimoto, T. Matsui, T. Okuda and S. Ichiba, *Chem. Lett.*, 1991, 801-804.
108. D. M. Trots and S. V. Myagkota, *J. Phys. Chem. Solids*, 2008, **69**, 2520-2526.
109. Y. Takahashi, R. Obara, Z. Z. Lin, T. Naito, T. Inabe, S. Ishibashi and K. Terakura, *Dalton Trans.*, 2011, **40**, 5563-5568.
110. K. Yamada, K. Nakada, Y. Takeuchi, K. Nawa and Y. Yamane, *Bull. Chem. Soc. Jpn.*, 2011, **84**, 926-932.
111. L. Guen, P. Palvadeau, M. Spiesser and M. Tournoux, *Revue De Chimie Minerale*, 1982, **19**, 1-10.
112. G. Thiele, H. W. Rotter and K. D. Schmidt, *Z. Anorg. Allg. Chem.*, 1987, **545**, 148-156.
113. N. Kitazawa, Y. Watanabe and Y. Nakamura, *J. Mater. Sci.*, 2002, **37**, 3585-3587.
114. Hayatullah, G. Murtaza, S. Muhammad, S. Naeem, M. N. Khalid and A. Manzar, *Acta Physica Polonica A*, 2013, **124**, 102-107.
115. E. Mosconi, A. Amat, M. K. Nazeeruddin, M. Gratzel and F. De Angelis, *J. Phys. Chem. C*, 2013, **117**, 13902-13913.
116. N. Onoda-Yamamuro, T. Matsuo and H. Suga, *J. Phys. Chem. Solids*, 1992, **53**, 935-939.
117. L.-y. Huang and W. R. L. Lambrecht, *Physical Review B*, 2013, **88**, 165203.
118. S. Colella, E. Mosconi, P. Fedeli, A. Listorti, F. Gazza, F. Orlandi, P. Ferro, T. Besagni, A. Rizzo, G. Calestani, G. Gigli, F. De Angelis and R. Mosca, *Chem. Mater.*, 2013, **25**, 4613-4618.
119. H. J. Snaith and L. Schmidt-Mende, *Adv. Mater. (Weinheim, Ger.)*, 2007, **19**, 3187-3200.
120. H. S. Kim, J. W. Lee, N. Yantara, P. P. Boix, S. A. Kulkarni, S. Mhaisalkar, M. Gratzel and N. G. Park, *Nano Lett.*, 2013, **13**, 2412-2417.
121. T. M. Koh, K. Fu, Y. Fang, S. Chen, T. C. Sum, N. Mathews, S. G. Mhaisalkar, P. P. Boix and T. Baikie, *The Journal of Physical Chemistry C*, 2013, 140117105541008.
122. S. Pang, H. Hu, J. Zhang, S. Lv, Y. Yu, F. Wei, T. Qin, H. Xu, Z. Liu and G. Cui, *Chem. Mater.*, 2014, **26**, 1485-1491.
123. D. Bi, L. Yang, G. Boschloo, A. Hagfeldt and E. M. J. Johansson, *The Journal of Physical Chemistry Letters*, 2013, **4**, 1532-1536.
124. N. J. Jeon, J. Lee, J. H. Noh, M. K. Nazeeruddin, M. Gratzel and S. I. Seok, *J. Am. Chem. Soc.*, 2013, **135**, 19087-19090.
125. J. A. Christians, R. C. Fung and P. V. Kamat, *J. Am. Chem. Soc.*, 2014, **136**, 758-764.
126. T. Krishnamoorthy, F. Kunwu, P. P. Boix, H. Li, T. M. Koh, W. L. Leong, S. Powar, A. Grimsdale, M. Grätzel, N. Mathews and S. G. Mhaisalkar, *Journal of Materials Chemistry A*, 2014.
127. Y. S. Kwon, J. Lim, H.-J. Yun, Y.-H. Kim and T. Park, *Energy & Environmental Science*, 2014, **7**, 1454.
128. S. Ito, S. Tanaka, H. Vahlman, H. Nishino, K. Manabe and P. Lund, *ChemPhysChem*, 2014, n/a-n/a.
129. C. Wehrenfennig, G. E. Eperon, M. B. Johnston, H. J. Snaith and L. M. Herz, *Adv. Mater. (Weinheim, Ger.)*, 2014, **26**, 1584-1589.
130. G. E. Eperon, V. M. Burlakov, A. Goriely and H. J. Snaith, *ACS Nano*, 2014, **8**, 591-598.
131. Q. Chen, H. Zhou, Z. Hong, S. Luo, H. S. Duan, H. H. Wang, Y. Liu, G. Li and Y. Yang, *J Am Chem Soc*, 2013.
132. G. Hodes and D. Cahen, *Nat. Photonics*, 2014, **8**, 87-88.

133. P. Audebert, G. Clavier, V. Alain-Rizzo, E. Deleporte, S. J. Zhang, J. S. Lauret, G. Lanty and C. Boissiere, *Chem. Mater.*, 2009, **21**, 210-214.

134. L. C. Schmidt, A. Pertegas, S. Gonzalez-Carrero, O. Malinkiewicz, S. Agouram, G. Minguez Espallargas, H. J. Bolink, R. E. Galian and J. Perez-Prieto, *J. Am. Chem. Soc.*, 2014, **136**, 850-853.

135. P. Qin, A. L. Domanski, A. K. Chandiran, R. Berger, H. J. Butt, M. I. Dar, T. Moehl, N. Tetreault, P. Gao, S. Ahmad, M. K. Nazeeruddin and M. Gratzel, *Nanoscale*, 2014, **6**, 1508-1514.

136. T. Leijtens, B. Lauber, G. E. Eperon, S. D. Stranks and H. J. Snaith, *The Journal of Physical Chemistry Letters*, 2014, 1096-1102.

137. A. Dualeh, N. Tétreault, T. Moehl, P. Gao, M. K. Nazeeruddin and M. Grätzel, *Adv. Funct. Mater.*, 2014, n/a-n/a.

138. P. Schulz, E. Edri, S. Kirmayer, G. Hodes, D. Cahen and A. Kahn, *Energy & Environmental Science*, 2014, **7**, 1377.

139. K. N. Liang, D. B. Mitzi and M. T. Prikas, *Chem. Mater.*, 1998, **10**, 403-411.

140. D. B. Mitzi, *Chem. Mater.*, 2001, **13**, 3283-3298.

141. D. B. Mitzi, M. T. Prikas and K. Chondroudis, *Chem. Mater.*, 1999, **11**, 542-+.

142. B. O'Regan and M. Grätzel, *Nature*, 1991, **353**, 737-740.

143. J. Bisquert, D. Cahen, G. Hodes, S. Ruhle and A. Zaban, *J. Phys. Chem. B*, 2004, **108**, 8106-8118.

144. M. A. Green, *Physica E-Low-Dimensional Systems & Nanostructures*, 2002, **14**, 11-17.

145. H. S. Kim, I. Mora-Sero, V. Gonzalez-Pedro, F. Fabregat-Santiago, E. J. Juarez-Perez, N. G. Park and J. Bisquert, *Nat Commun*, 2013, **4**, 2242.

146. N. G. Park, *Journal of Physical Chemistry Letters*, 2013, **4**, 2423-2429.

147. H. J. Snaith, *Journal of Physical Chemistry Letters*, 2013, **4**, 3623-3630.

148. H. Li, K. Fu, A. Hagfeldt, M. Gratzel, S. G. Mhaisalkar and A. C. Grimsdale, *Angew Chem Int Ed Engl*, 2014, n/a-n/a.

149. J. Y. Jeng, Y. F. Chiang, M. H. Lee, S. R. Peng, T. F. Guo, P. Chen and T. C. Wen, *Adv Mater*, 2013, **25**, 3727-3732.

150. M. H. Kumar, N. Yantara, S. Dharani, M. Graetzel, S. Mhaisalkar, P. P. Boix and N. Mathews, *Chem Commun (Camb)*, 2013, **49**, 11089-11091.

151. E. J. Juarez-Perez, M. Wuβler, F. Fabregat-Santiago, K. Lakus-Wollny, E. Mankel, T. Mayer, W. Jaegermann and I. Mora-Sero, *The Journal of Physical Chemistry Letters*, 2014, **5**, 680-685.

152. V. Gonzalez-Pedro, E. J. Juarez-Perez, W. S. Arsyad, E. M. Barea, F. Fabregat-Santiago, I. Mora-Sero and J. Bisquert, *Nano Lett.*, 2014, **14**, 888-893.

153. Y. Zhao, A. M. Nardes and K. Zhu, *The Journal of Physical Chemistry Letters*, 2014, **5**, 490-494.

154. Y. Zhao and K. Zhu, *The Journal of Physical Chemistry Letters*, 2013, **4**, 2880-2884.

155. G. Giorgi, J. I. Fujisawa, H. Segawa and K. Yamashita, *Journal of Physical Chemistry Letters*, 2013, **4**, 4213-4216.

156. A. M. Goodman and A. Rose, *J. Appl. Phys.*, 1971, **42**, 2823-&.

157. V. D. Mihailetchi, J. Wildeman and P. W. Blom, *Phys. Rev. Lett.*, 2005, **94**, 126602.

158. L. J. A. Koster, V. D. Mihailetchi, H. Xie and P. W. M. Blom, *Appl. Phys. Lett.*, 2005, **87**.

159. J. M. Frost, K. T. Butler, F. Brivio, C. H. Hendon, M. van Schilfgaarde and A. Walsh, *Nano Lett.*, 2014.

160. C. S. Ponseca, Jr., T. J. Savenije, M. Abdellah, K. Zheng, A. Yartsev, T. Pascher, T. Harlang, P. Chabera, T. Pullerits, A. Stepanov, J. P. Wolf and V. Sundstrom, *J. Am. Chem. Soc.*, 2014, **136**, 5189-5192.

Table of Contents

This review presents the state-of-the-art Organohalide Lead Perovskites, which are currently making an immense impact across the photovoltaic community.